



Full Text View

[Volume 29, Issue 8 \(August 1999\)](#)

Journal of Physical Oceanography

Article: pp. 1772–1786 | [Abstract](#) | [PDF \(270K\)](#)

Stochastically Forced Mode Water Variability

W. Hazeleger and S. S. Drijfhout

Royal Netherlands Meteorological Institute, De Bilt, the Netherlands

(Manuscript received September 3, 1997, in final form August 7, 1998)

DOI: 10.1175/1520-0485(1999)029<1772:SFMWV>2.0.CO;2

ABSTRACT

Substantial interannual to decadal variability is observed in the properties of subtropical mode water of the North Atlantic. In this study the response of mode water to stochastic atmospheric forcing is investigated in a numerical model.

In a series of experiments the response is studied to different components of stochastic atmospheric forcing, such as wind stress, freshwater flux, and heat flux. The numerical model consists of an isopycnal ocean model with explicit mixed layer physics. The stochastic forcing is superimposed on the climatological forcing. The stochastic forcing function has an idealized form, but the amplitude, the spatial, and the temporal variability are based on observations. When a stochastic heat flux is applied, an atmospheric anomaly model is coupled to the ocean model. The geometry of the model is idealized and mimics the subtropical gyre of the North Atlantic.

The stochastic wind stress forcing excites an internal mode in the mode water layer of the model. The response is characterized by the propagation of baroclinic waves. The spectrum of the response to stochastic freshwater flux is red.

In the coupled model the stochastic heat flux forcing generates variability characterized by a dipole pattern in the mode water. The spectrum of the response is red and dominates the response to the stochastic wind stress and freshwater flux. The response is damped by an atmospheric feedback that consists of anomalous heat fluxes, depending on the SST anomalies generated by the stochastic forcing itself.

Only stochastic heat flux forcing can generate mode water variability of the observed amplitude. A preferred timescale in mode water variability should be contained in the forcing itself or it may result from modes that could not be simulated by the present model.

Table of Contents:

- [Introduction](#)
- [Numerical model and forcing](#)
- [Stochastic forcing experiments](#)
- [Summary and conclusions](#)
- [REFERENCES](#)
- [APPENDIX](#)
- [FIGURES](#)

Options:

- [Create Reference](#)
- [Email this Article](#)
- [Add to MyArchive](#)
- [Search AMS Glossary](#)

Search CrossRef for:

- [Articles Citing This Article](#)

Search Google Scholar for:

- [W. Hazeleger](#)
- [S. S. Drijfhout](#)

1. Introduction

The climate system exhibits variability on many timescales. However, the spectra of continuous climate time series tend to have increasing variance at decreasing frequency. The mechanisms for generating low-frequency climate variability are not clear and are the subject of many present-day climate studies.

A possible mechanism for climate variability has been presented by [Hasselmann \(1976\)](#). In his stochastic climate model, the climate system is described as a slowly evolving subsystem forced by high-frequency weather fluctuations. The model describes a random walk process. The variance of the slowly evolving climate variables (e.g., ocean properties) grows in time, which results in red noise spectra. At low frequencies climate spectra flatten due to dissipation or negative feedback processes.

Observed climate spectra exhibit peaks above the red noise spectrum. These peaks may be the result of internal resonances or positive feedback processes. Stochastic forcing can excite internal modes of variability that are linearly damped oscillatory eigenmodes under steady forcing ([Griffies and Tziperman 1995](#)). Furthermore, spatial resonances between dominant modes of surface fluxes and oceanic modes may excite internal oceanic variability as shown by [Saravanan and McWilliams \(1997\)](#). [Saravanan and McWilliams \(1998\)](#) showed that peaks may arise when ocean advection and coherent atmospheric forcing are considered in Hasselmann's model. The variability is generated when nonlocal advective effects dominate the local damping. In their analytical model no intrinsic oscillatory modes are necessary to generate peaks in climate spectra.

The stochastic climate model has been used in many studies as a framework to investigate low-frequency variability of the ocean (e.g., [Hall and Manabe 1997](#)). Also, the ability of the forcing to excite internal modes of variability in the ocean has been investigated (e.g., [Weisse et al. 1994](#)). In the present study, the concept of stochastic climate models is applied to investigate variability in subtropical mode water. Subtropical mode water (henceforth mode water) is a subsurface water mass characterized by its vertical homogeneity in temperature and salinity. At Panulirus Station, near Bermuda pronounced interannual to decadal variability in mode water is observed ([Talley and Raymer 1982](#); [Joyce and Robbins 1996](#)).

Mode water is formed south of the Gulf Stream extension by subduction from the mixed layer. During spring when the mixed layer detrains, well-mixed water transfers to the thermocline. Since the mixed layer depth is largely determined by surface fluxes, local air–sea interaction might generate mode water variability. [Talley and Raymer \(1982\)](#) related the observed mode water variability to the observed variability in the heat flux in the formation region of mode water. A weak correlation was found, which led to the speculation that a storage mechanism might be operative. [Dickson et al. \(1996\)](#) suggested that convection in the Labrador, Greenland, and Sargasso Seas is driven by large-scale atmospheric variability. The dominant mode of variability of the atmosphere in the North Atlantic region is characterized by a dipole pattern in the pressure distribution. This mode is known as the North Atlantic oscillation (NAO). [Hazeleger and Drijfhout \(1998, hereafter HD98\)](#) investigated mode water variability in relation to the NAO. A numerical ocean model was forced with anomalous forcing of the observed amplitude and timescale. The response of the mode water in the model was realistic. Local air–sea interaction mechanisms in conjunction with the storage mechanism could explain the response. However, discrepancies between model results and observations remained. Also, it was not clear to what extent other physical mechanisms could generate a similar response.

In the present study, an isopycnic primitive equation model of an idealized North Atlantic subtropical gyre is used. The model includes mixed layer physics and is coupled to an atmospheric anomaly model. The model is driven by a stochastic forcing superimposed on the climatological forcing. Experiments are performed with a stochastic wind stress, a stochastic freshwater flux, and a stochastic heat flux, both separately and together. The amplitude and decorrelation time of the stochastic forcing are estimated from observed variations in the wind, precipitation, and heat flux. In this study we assess the contribution of this type of air–sea interaction to the observed mode water variability. Spatial and temporal variability in the mode water layer of the numerical model is analyzed within the framework of stochastic climate models. Furthermore, the results are compared with the response to anomalous forcings in the same model as presented by HD98.

In the next section the numerical ocean model, the atmospheric anomaly model, and the stochastic forcing are described. The results of the integrations with the different stochastic forcing types are presented in [section 3](#). In [section 3a](#) the response to stochastic wind stress forcing is discussed and in [section 3b](#) the results of the stochastic freshwater flux forcing experiment are presented. The results of the integration with a stochastic heat flux is discussed in [section 3c](#). In [section 4](#) the results are summarized and conclusions are drawn.

2. Numerical model and forcing

a. The ocean model

Mode water is a distinct water mass. The advantage of layer models, among others, is the unambiguous definition of water masses. In this study we use an isopycnic primitive equation ocean model. The model is based on the isopycnic model of [Bleck et al. \(1989\)](#). The model has been described by [Drijfhout \(1994\)](#) and HD98. The version used in this study has seven isopycnic layers. Because mode water is formed by subduction from the mixed layer, a nonisopycnic bulk mixed layer is coupled to the isopycnic model according to [Bleck et al. \(1989\)](#).

A linear equation of state is used. In the experiment with a stochastic wind stress forcing, salinity is kept constant. The density difference between the isopycnal layers is equivalent to a temperature difference of 4°C. The deepest layer has a temperature of 2°C. In the experiments that include a stochastic freshwater flux, salinity is allowed to vary. In the isopycnal layers salinity is advected and diffused. By the constraint of density conservation in the isopycnal layers, temperature is calculated as a residual ([Bleck et al. 1992](#)). The density differences between the isopycnal layers are the same as in the isothermal version of the model. The geometry of the model is idealized. The rectangular domain (e.g., [Fig. 1](#) and HD98) captures the main features of the North Atlantic subtropical gyre. Due to the coarse horizontal resolution (74 km) eddies are not resolved. The maximum depth is 4000 m. At the western boundary topography mimics the continental shelf break (see [Drijfhout 1994](#)).

In the uncoupled version of the model, the temperature is restored to a zonally averaged, seasonal varying apparent temperature. The restoring timescale for SST is 20 days for a mixed layer of 50 m, otherwise proportional to the mixed layer depth. In some experiments a freshwater flux is diagnosed from an additional spinup with restoring boundary conditions for salinity. The same restoring timescale as for temperature was chosen. This is a very rudimentary way to parameterize the buoyancy fluxes. It mimics that the SST feeds back on the heat flux, while sea surface salinity does not affect the freshwater flux.

We refer to HD98 for a detailed discussion on the limitations of the model. Among the shortcomings of the model is the small domain. At the latitude of the Gulf Stream, the basin is three times smaller than the real Atlantic basin. In order to obtain a realistic transport and advective timescale in the gyre we increased the wind stress by a factor of 3 and shortened the seasonal cycle correspondingly. This will lead to an increase in instantaneous Ekman pumping and subduction. However, due to the shortened seasonal cycle, the actual transferred amount of water between the mixed layer and the subsurface layers will be correct. When applying a stochastic forcing, the shortening of the seasonal cycle has been taken into account.

The version of the model including salinity variations was initialized from the equilibrium state (1000 years spinup) of the isothermal model with a constant salinity of 35 psu. The model was spun up under restoring boundary conditions for salinity and temperature for an extra 200 years. Then, the freshwater flux was diagnosed and the model was run with mixed boundary conditions for another 200 years. No internal variability occurred during the additional spinup. The sea surface salinity of the equilibrium state is shown in [Fig. 1](#). The main features of the observed salinity distribution in the North Atlantic subtropical gyre are present. There is a gradient at the latitude of the Gulf Stream. A pool with high salinities is found in the subtropical gyre. Note that the maximum salinity in the subtropics is smaller than observed (36.1 psu instead of 36.5 psu). This is caused by the small, closed basin and the demand that the integrated freshwater flux has to vanish to ensure salinity conservation. This implies a strong freshwater flux in the north. The forcing is chosen to yield a realistic gradient. In reality, the freshwater flux at the surface is negative for this region. This is compensated by a freshwater transport through the boundaries. Such a freshwater balance cannot be simulated by the present model.

In the isothermal version of the model the 18°C layer is the thickest subsurface layer. The layer covers the subtropical gyre. The outcrop of the 18°C layer is positioned near the Gulf Stream front. This layer is the model equivalent of mode water. For further details on the parameters of the ocean model and general features of the model solution, we refer to HD98.

b. The atmospheric anomaly model

The restoring boundary conditions for the heat flux strongly damp SST anomalies. In order to model air–sea interaction in a more realistic way, an atmospheric anomaly model is coupled to the ocean model according to [Luksch and von Storch \(1992\)](#). In this model the SST anomalies feed back to the thermal forcing.

In the coupled model the ocean is forced with climatological mean heat fluxes modified by air temperature tendencies. The mean heat fluxes are diagnosed after the spinup with restoring boundary conditions ([Fig. 2](#)). The mean heat flux shows cooling in the Gulf Stream region and in the North. The amplitude of the forcing is close to observations (see [Wright 1988](#)). The anomalous air temperature tendencies are derived using an advective model for the atmosphere ([Luksch and von Storch 1992](#)):

$$\partial t \quad \mathbf{u}_a \quad \mathbf{v}_a \quad \mathbf{w}_a \quad \mathbf{v}(\mathbf{x}_a, t_a) \quad \rho_a c_{pa} H_A$$

$$+ \kappa \nabla^2 T'_a. \quad (1)$$

Here, the subscript a applies to atmospheric quantities. Anomalies are denoted by a prime. A diffusion of T'_a is incorporated to parameterize unresolved processes. The diffusivity is $\kappa = 1.6 \times 10^4 \text{ m s}^{-1}$; ρ_a is the density of air, c_{pa} the specific heat of air, and H_A is the height of the homogeneous atmosphere. The latter is the height of the atmospheric mixed layer, which is typically 1000 m. The anomalous air temperature is forced by an anomalous heat flux, which is determined with a drag relation:

$$Q'_H = \rho_a c_{pa} c_H \mathbf{e} |\mathbf{u}_a| (T'_a - T'_{oc}), \quad (2)$$

where $c_H = 1.3 \times 10^{-3}$ is the drag coefficient and T'_{oc} is the difference between the simulated SST and the SST diagnosed after the spinup. Here \mathbf{e} is the ratio of the total heat flux to the sensible heat flux, which is chosen to be 4 (see [Drijfhout and Walsteijn 1998](#)). The same anomalous heat flux (of the opposite sign) is added to the mean heat flux forcing to force the temperature in the mixed layer of the ocean. The atmospheric wind consists of a mean part \mathbf{u}_a and an anomalous part \mathbf{u}'_a , which is obtained by the thermal wind relation:

$$u'_a = -\frac{R}{f} \left(\frac{\partial T'_a}{\partial y} \right)_p \ln \left(\frac{p_0}{p_1} \right) \quad (3)$$

$$v'_a = \frac{R}{f} \left(\frac{\partial T'_a}{\partial x} \right)_p \ln \left(\frac{p_0}{p_1} \right). \quad (4)$$

Here R is the gas constant for dry air, f is the Coriolis parameter, p_0 is the surface pressure, and p_1 is the pressure at height H_A . We assume that the temperature anomalies vanish above 1000 m (H_A). We calculate an anomalous wind stress to force the ocean model from the anomalous wind. This process was not incorporated by [Drijfhout and Walsteijn \(1998\)](#). The anomalous wind stress is derived using a drag relation with a drag coefficient $C_D = 1.44 \times 10^{-3}$; that is,

$$\tau_x = \rho C_D |\mathbf{u}_a| u_a, \quad \tau_y = \rho C_D |\mathbf{u}_a| v_a. \quad (5)$$

More details on the atmospheric part of the model can be found in [Drijfhout and Walsteijn \(1998\)](#) and [Luksch and von Storch \(1992\)](#).

c. The stochastic forcing

In general, short-term variability in air–sea interaction in the midlatitudes is caused by baroclinic disturbances in the atmosphere. These structures have a period of several days and a wavelength of 3000–6000 km. At periods longer than 10–20 days the spectra of atmospheric variables are white.

[Saravanan and McWilliams \(1997\)](#) point out that (inter)decadal variability may be excited by a temporally random, but spatially correlated forcing. Furthermore, [Jin \(1997\)](#) showed that the response of the ocean is a function of the wavenumber of the applied forcing. The most dominant atmospheric patterns of variability in the North Atlantic correspond to the NAO. These basin-scale patterns seem to be intrinsically generated in the atmosphere ([Selten et al. 1999](#)). Therefore, we applied a spatially correlated pattern with a wavenumber that varies between 0.5 and 1.5. The amplitude and phase are white noise in time. This results in a variety of correlated patterns. Due to the random phase, the patterns propagate on short timescales. This mimics the propagating baroclinic disturbances. On average the patterns are sinusoidal, which mimics the NAO and a few higher harmonics. Among the patterns, one that projects well on the observed forcing patterns is likely to be generated. This idealized approach may lead to an underrated response to stochastic forcing. Another approach is to derive the atmospheric variability from a coupled model. However, the model configuration is too idealized to perform such an experiment.

In order to resolve the spatial correlative and temporal random features of the stochastic forcing, a linear combination of a

few sinusoids is used; that is,

$$\mathcal{F}(x, y, t) = \sum_{i=1}^2 \sum_{j=1}^3 Z_{ij}(t) \left(\sin \frac{ix\pi}{L_x} + \phi_{ij}(t) \right) \times \left(\sin \frac{jy\pi}{L_y} + \phi_{ij}(t) \right), \quad (6)$$

where \mathcal{F} is the forcing (wind stress, freshwater flux, or heat flux), L_x is the zonal extension of the domain, L_y is the meridional extension of the domain, Z is a random amplitude, and ϕ is a random phase. Similar stochastic forcing functions have been used by other authors (e.g., [Capotondi and Holland 1997](#); [Jin 1997](#)).

In the stochastic wind stress experiments the random coefficients are updated every 5 days. This is a typical timescale for baroclinic disturbances in the atmosphere to develop and dissipate. The observed standard deviation of the scalar wind over the North Atlantic region is 4 m s^{-1} ([Wright 1988](#)). Using a drag relation the variance in the wind stress can be estimated:

$$\sigma_\tau^2 = 3C_D^2 \sigma_u^4. \quad (7)$$

Here C_D is the drag coefficient and σ_u is the standard deviation of the wind speed. From [Eq. \(7\)](#), the standard deviation of the stochastic wind stress forcing is found to be 0.2 N m^{-2} . The spectral characteristics of the idealized stochastic forcing resembles the characteristics of the observed atmospheric forcing. In [Fig. 3](#), a spectrum of the wind stress observed during the subduction experiment is shown (N. Brink 1997, personal communication), together with a spectrum derived from the stochastic forcing function. Both spectra flatten beyond a timescale of 10 days and have a comparable white noise level.

For the freshwater flux a value of $100 \text{ mm month}^{-1}$ with a decorrelation time of 3 h is taken. This is a typical value for a subtropical station ([Dorman et al. 1974](#)).

When the ocean is driven by restoring boundary conditions for SST, stochastic fluctuations in the heat flux will be strongly damped. Therefore, a stochastic heat flux forcing is only applied when the ocean model is coupled to the atmospheric anomaly model. [Fissel et al. \(1976\)](#) report that variability in the heat flux peaks at synoptic timescales. Therefore, the same decorrelation timescale as for wind stress anomalies (5 days) is chosen. We have chosen to vary the amplitude of the stochastic heat flux forcing with the seasonal cycle. The amplitude is multiplied by a constant, which varies between 1 in the winter and 0.5 in the summer. The twice as low amplitude results in a four times weaker variance during summer. This is in accordance with observations (see [Fissel et al. 1976](#), Table 2). The standard deviation of the applied heat flux is 65 W m^{-2} . The stochastic forcing in the wind stress and the freshwater flux have a less pronounced seasonal cycle ([Fissel et al. 1976](#)). Therefore, we have neglected the seasonal cycle in the stochastic forcing for these components.

The stochastic forcing in the wind stress is superimposed on the climatological mean forcing. In the stochastic freshwater flux experiment the buoyancy forcing is

$$B = -\frac{g}{\rho_0} [a\gamma(T_s - T) - bS_0((E - P) + \mathcal{F}_{E-P})], \quad (8)$$

with γ the restoring timescale, T_s the apparent temperature, S_0 the mean salinity, $(E - P)$ the freshwater flux, and \mathcal{F}_{E-P} is the stochastic freshwater flux; a and b are the expansion coefficients for temperature and salinity, respectively.

In the coupled model the buoyancy forcing is

$$B = -\frac{g}{\rho_0} \left(\frac{a(Q_{\text{obs}} + Q'_H + \mathcal{F}_Q)}{c_p} - bS_0(E - P) \right), \quad (9)$$

where Q_{obs} is the diagnosed heat flux from the run with restoring boundary conditions (see [Fig. 2](#)) and \mathcal{F}_Q is the stochastic heat flux forcing. Using these stochastic forcings we investigate to which extent the theory of [Hasselmann \(1976\)](#)

can account for mode water variability. Furthermore, we explore the nature of internal modes excited by the stochastic forcing.

3. Stochastic forcing experiments

After the spinup to a cyclo-stationary state, the stochastic forcing was applied. In the experiments with the ocean-only model the stochastic forcing has been applied for 140 years. In the coupled model substantial variability on the decadal timescale occurred. In that case, the integration was continued to 300 years in order to resolve possible decadal modes of variability.

The analysis of the variability induced by the forcing is based on monthly mean values. In order to allow the upper layers to adjust after the new forcing was applied, the first 40 years of the integration have been omitted in the analysis. For each calendar month the linear trend for the complete integration has been subtracted from the data. Then, the average of each calendar month is determined and subtracted from the detrended monthly means to produce monthly anomaly fields. This study focuses on interannual to decadal variability. Therefore, finally a 1-yr running mean was performed to remove high-frequency variability. The running mean smooths the data, but the sampling is still monthly. The layer thickness is the most natural variable to analyze in isopycnic models. Here, we focus on the thickness variations of the mode water layer.

a. Stochastic wind stress experiment

The stochastic wind stress forcing affects the mode water layer in primarily two ways. First, the stochastic forcing leads to anomalous (isopycnal) convergence, which induces anomalous Ekman pumping. Second, the forcing affects the turbulent kinetic energy budget of the mixed layer. The stochastic wind stress forcing drives anomalous (diapycnal) mass fluxes between the mixed layer and the ventilated thermocline by anomalous entrainment and detrainment. Both processes are equally efficient in producing thickness anomalies in the mode water layer (see [section 3b](#)).

In the stochastic wind stress experiment the maximum standard deviation of the thickness of the mode water layer is 5 m. The thickness anomalies resemble the anomalies generated by a large-scale, low-frequency anomalous wind stress (see HD98). Maximum thickness anomalies of 10 m are generated by the stochastic forcing, which is the same order of magnitude as in the generic wind stress experiment. The monthly mean stochastic forcing is two orders of magnitude smaller than the monthly mean generic wind stress forcing. This implies that the ocean integrates the white noise forcing in accordance with the stochastic climate model.

To study spatial and temporal variability of mode water thickness in more detail, empirical orthogonal functions (EOFs) of the mode water thickness are computed. The spectrum of the principal components of the leading EOF is shown in [Fig. 4](#). The confidence intervals are based on 30 000 spectra of first-order autoregressive processes (the idealized red noise response) with a variance and lag-one correlation of the unfiltered time series itself. The spectrum of the slowly evolving component of the idealized stochastic climate model is

$$F_T(\omega) = \frac{F_f}{\omega^2 + \lambda^2}, \quad (10)$$

where ω is the frequency, λ is the feedback factor, and F_f is the constant spectrum of the white noise forcing. This spectrum indicates that the spectral density increases with decreasing frequency. At a frequency of $\omega \ll \lambda$ the spectrum approaches a constant value. Although the stochastic climate model applies formally to local forcing and response, the theory is applicable to integrated variables (EOF time series) as well.

The spectrum shown in [Fig. 4](#) is consistent with the stochastic climate model. The variance increases until a frequency of 9 yr^{-1} . At low frequencies a significant deviation from the idealized stochastic model occurs, as demonstrated by the broad peak at a period of 7 yr. The leading EOF is not very dominant. The first five EOFs account for 28%, 23%, 13%, 10%, and 7% of the variance, respectively. All EOF spectra display a peak around 7 years (not shown).

The EOF patterns have signatures of wavelike phenomena (not shown). The patterns in the westward return flow are comparable to the patterns of thickness anomalies induced by a deterministic anomalous wind stress (see Fig. 19, HD98). There, these patterns were identified as baroclinic waves. With EOF analysis, only standing oscillations can be resolved. EOFs are not optimized to identify highly predictive flow structures, such as propagating waves. Therefore, optimal autocorrelation functions (OAFs) are constructed ([Selten et al. 1999](#), see also appendix). OAFs are derived by maximizing the autocorrelation of a linear combination of the principal components of the EOFs. An oscillation is represented by a pair of eigenvectors (OAF patterns) and principal components that have the same dominant frequency and are dephased by one-quarter period.

The eigenvalues of the OAFs at different time lags are shown in [Fig. 5](#). The minimal autocorrelation of OAF 4 and 5 at a period of 25 months implies the possibility of a propagating feature. The period (4×25 months ≈ 8 yr) corresponds to the broad peak in the spectra of the EOFs. The anomaly patterns associated with OAF 4 and 5 are recovered by the sum of the OAF patterns multiplied by their principal components. Snapshots of the evolution of the anomalies are shown in [Fig. 6](#). The thickness anomalies propagate westward in the subtropical gyre. The patterns are identified as long baroclinic waves. Such anomalies have been described by HD98. The stochastic wind stress forcing leads to a continuous excitation of the anomalies at the eastern boundary. The anomalies follow the westward return flow and amplify due to the continuous input of energy by the wind. These mechanisms have been clarified by [Jin \(1997\)](#) and [Frankignoul et al. \(1997\)](#). When the anomalies arrive at the southwestern boundary, they propagate rapidly into the western boundary current region. The anomalies dissipate in this region; no reflection takes place.

The westward propagation is well visible in a time–latitude diagram of the thickness anomalies ([Fig. 7a](#)). The propagation speed of the anomalies is approximately 4.2 cm s^{-1} . Using the simulated vertical structure of the density along this section, the theoretical Rossby wave speed of the first baroclinic mode is $c_1 = \beta g h_1 / f_0^2 \approx 2.9 \text{ cm s}^{-1}$ [the equivalent depth h_1 is determined according to [Flierl \(1978\)](#), see [Fig. 7b](#)]. The mean westward velocity is 1.2 cm s^{-1} . So, the simulated wave speed matches well with the theoretically derived wave speed. In the idealized model of Frankignoul et al. the anomalies move with twice the Rossby wave speed. This is not observed in our model. The timescale of the variability found by Frankignoul et al. is determined by the wave speed and the width of the basin. This is also the case in the present model. The vertical structure of the anomalies indicated a first baroclinic mode (not shown).

b. Stochastic freshwater flux experiment

A nonhomogeneous freshwater flux generates density anomalies in the mixed layer. The associated anomalous pressure gradients on the isopycnal surfaces can induce thickness anomalies in the mode water layer. Furthermore, the buoyancy fluxes affect the turbulent kinetic energy budget in the mixed layer. Thus, stochastic buoyancy forcing may also induce thickness anomalies in the mode water layer by anomalous entrainment and detrainment from the mixed layer. In addition, stochastic freshwater flux affects the stability of the water column.

The maximum standard deviation of the mode water thickness in the experiment with stochastic freshwater flux is 3 m. The highest standard deviation is found near the outcrop of the 18°C layer. This indicates a local, passive response of the ocean. At the outcrop mode water is locally formed by subduction from the mixed layer. Variability arises easily at the outcrop as a response to a varying buoyancy forcing. The pattern of the leading EOF displays the variability as described above ([Fig. 8](#)). The first EOF accounts for 41% of the variance. The dominance suggests that anomalous subduction determines the variability in the mode water layer in this experiment.

The spectrum of the leading EOF of the mode water thickness anomalies ([Fig. 9](#)) demonstrates that the ocean integrates the white noise forcing. No peaks arise above the 95% confidence level. Although the spectrum does not flatten yet, the run has not been continued because the amplitude of the response is too small to play an important role in mode water variability.

The response of the mode water layer differs from the response in the stochastic wind stress experiment. The amplitudes of the response are comparable, but stochastic wind stress forcing induces a traveling mode. In that experiment, no dominant EOF is found. The response to the stochastic freshwater flux forcing is passive. The dominance of the leading EOF and the red spectrum implies a standing mode without a dominant timescale. In order to explain the differences between the two experiments, the contribution of both types of stochastic forcing to the vertical velocity at the base of the mixed layer is estimated. This is a suitable measure because mode water usually compensates for changes in the mixed layer thickness.

We follow the analytical approach of [Frankignoul and Müller \(1979\)](#) in estimating the relative importance of the different forcing types. First, the vertical mass flux due the divergence of the horizontal mass flux is estimated. A homogeneous mixed layer is considered that is forced by a fluctuating wind stress and buoyancy flux. The vertical velocity at the base of the mixed layer associated with the surface forcing can be obtained [see [Frankignoul and Müller \(1979\)](#) for details on the derivation]:

$$w_{H_0}^{(1)} = \frac{H_0}{2f_0^2} \left(\nabla^2 + \beta \left(\frac{\partial}{\partial t} \right)^{-1} \frac{\partial}{\partial x} \right) B + \frac{1}{\rho_0 f_0} \mathbf{k} \cdot \nabla \times \boldsymbol{\tau}, \quad (11)$$


where H_0 is the mixed layer depth, B is the buoyancy forcing [[Eq.\(8\)](#)], and $\boldsymbol{\tau}$ is the wind stress forcing. The first term on the right-hand side of [\(11\)](#) represents the vertical velocity induced by nonhomogeneities in the buoyancy flux. The second

term can be recognized as the Ekman pumping.

The surface forcing induces an extra vertical velocity if mixed layer physics are taken into account. This entrainment velocity is determined by the turbulent kinetic energy budget in the bulk mixed layer formulation (see [Bleck et al. 1989](#)):

$$w_{H_0}^{(2)} = \frac{(2/H_0)mu_*^3 + nB}{\Delta b}, \quad (12)$$


with m and n the dissipation parameters, $u_* = ((\tau/\rho_0))^{1/2}$, and Δb the buoyancy difference between the mixed layer and the underlying isopycnic layer.

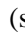

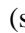


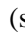
The direct contribution of the different stochastic forcing types to the vertical velocity can be estimated from [Eqs. \(11\)](#) and [\(12\)](#). The white noise levels of the spectra of the stochastic forcings are used as a characteristic measure of the stochastic forcing (e.g., [Fig. 3](#) ). Since the same spatial structure for stochastic wind stress and freshwater flux forcing is used, the wavenumber–frequency spectrum is replaced by the frequency (power) spectrum.

The relative importance of the stochastic wind stress forcing with respect to the stochastic freshwater flux is estimated from the ratio of the terms involving the wind stress to the terms involving the buoyancy flux in [\(11\)](#) and [\(12\)](#) due to the freshwater flux forcing:

$$\frac{(2f_0k)^2F_\tau(0) + [2m/(H_0\Delta b)]^2F_{u_*^3}(0)}{\{(H_0gbS_0)^2(k^2 + \beta k/\omega)^2 + [ngb/(\rho_0\Delta b)]^2\}F_{E-P}(0)} \approx 1.7. \quad (13)$$

As we focus on gyre-scale structures and interannual variability, we have chosen for the wavenumber $k = (2\pi/1000)$ km^{-1} and for the frequency $\omega = (2\pi/6)$ yr^{-1} . Furthermore, $f_0 = 0.9 \times 10^{-4}$ s^{-1} , $H_0 = 100$ m, $\beta = 2 \times 10^{-11}$ s^{-1} m^{-1} , $b = 7.7 \times 10^{-4}$ kg m^{-3} psu^{-1} , $S_0 = 35$ psu, $g = 10$ m s^{-2} , $n = 0.4$, and $\Delta b = 4 \times 10^{-3}$ kg m^{-2} s^{-2} (equivalent to a temperature difference between the mixed layer and the underlying isopycnal layer of 2°C). These numbers correspond with parameters in the numerical model and the position of anomalies in the mode water layer. The white noise levels of the spectra of the stochastic freshwater flux water forcing and wind stress forcing are $F_{E-P}(0) = 1 \times 10^{-7}$ $\text{m}^2 \text{s}^{-2}$, $F_\tau(0) = 1 \times 10^{-2}$ $\text{N}^2 \text{m}^{-4}$, and $F_{u_*^3}(0) = 5 \times 10^{-13}$ $\text{m}^6 \text{s}^{-6}$.

The ratio of the variances [\(13\)](#) shows that the contribution of the stochastic wind stress dominates slightly over the contribution of the stochastic freshwater flux. Obviously, the ratio [\(13\)](#) depends on the choice of various parameters. In [Fig. 10](#)  the value of the ratio is shown with respect to wavenumber and period. The freshwater flux appears to be more efficient at lower frequencies and larger wavelengths. It can easily be verified that the contribution of the Ekman pumping and the turbulent freshwater fluxes is of the same order of magnitude. The contribution of the divergence of the flow by the freshwater fluxes [first term in [Eq. \(11\)](#)] is an order of magnitude smaller.

The estimates confirm the results of the experiments with the numerical model. The standard deviations of the mode water thickness in the stochastic wind stress and freshwater flux experiment have the same order of magnitude. The spectral powers are comparable (see [Figs. 4](#)  and [9](#) ). In [Fig. 4](#)  there is a significant peak associated with a traveling mode. [Figure 9](#)  displays a red spectrum associated with a standing mode. On smaller scales the contribution of the wind stress becomes more important than the freshwater fluxes ([Fig. 10](#) ). The anomaly patterns in the stochastic wind stress experiment are indeed smaller than the basin-scale anomaly pattern generated in the stochastic freshwater flux experiment. This may explain the traveling mode associated with the peak in [Fig. 4](#) .

Results of an experiment with both a stochastic wind stress and freshwater flux forcing did not exhibit new features. In the pattern of the first EOF, there are signatures of the stochastic freshwater flux as well as of planetary waves (not shown). The spectra of the EOF time series peak at 7 years and the same wind stress generated patterns as presented in [section 3a](#) are recovered with OAF analysis (not shown).

c. Stochastic heat flux in the coupled model

SST anomalies induced by a stochastic heat flux are strongly damped when mixed boundary conditions are used. In the

coupled model air–sea interaction is modeled realistically. After the atmospheric anomaly model was coupled to the ocean model, adjustment of the ocean took place [see [Drijfhout and Walsteijn \(1998\)](#) for a comparison between an uncoupled and a coupled version of the model]. The new ocean climate, however, differs not much from the climate obtained after the uncoupled run. Without stochastic forcing this simple coupled model shows no internal variability. After 40 years of integration in the coupled model a stochastic heat flux forcing was applied.

The response of the mode water layer to the stochastic heat flux is significant. The maximum standard deviation is 10 m. Large thickness anomalies (maxima of 25 m) are found in the mode water layer in the center of the subtropical gyre. [Figure 11](#) shows a time series of potential vorticity anomalies obtained from the stochastic heat flux forcing experiment. The position in the center of the subtropical gyre (25°N, 76°W) is chosen to correspond with Panulirus Station. [Talley and Raymer \(1982\)](#) observed potential vorticity anomalies of approximately $50 \times 10^{-14} \text{ cm}^{-1} \text{ s}^{-1}$ at Panulirus.¹ The amplitude of the variability is comparable to the response to deterministic heat flux forcing in the model study of HD98.

To study coupled variability, singular value decomposition (SVD) has been applied to EOFs of the mode water thickness and the anomalous heat flux Q'_H [Eq. (2)]. SVD analysis selects dominant coupled patterns of variability. The first SVD mode accounts for 66% of the squared covariance. The spectrum of the principal components of the oceanic part is shown in [Fig. 12](#). Although substantial variability on the decadal timescale is generated, no peaks arise above the red noise spectrum.

The SVDs are determined at different lags. This involves the covariance matrix between the time series of the EOFs of mode water thickness and anomalous heat flux (Q'_H) at different lags. The correlations between the time series of the SVDs at different lags are determined for the first and second SVD mode (together they account for more than 90% of the squared covariance). The lags can be interpreted as response times of the ocean. [Figure 13](#) shows a maximum in the correlation between the time series of the first SVD at a lag of 13 months (Q'_H leads). The second SVD has a maximum correlation at a lag of 5 months. These response times are the result of air–sea interaction and subduction processes.

At a response time of 13 months, a dipole pattern in the oceanic part of the SVD is present ([Fig. 14a](#)). The large positive thickness anomaly is associated with cooling. Water from lighter and warmer layers is transferred to cooler and deeper layers (see also HD98). The lagged SVD analysis of SST and mode water thickness at a lag of 13 months (SST leads) confirmed that anomalous low SSTs are associated with the positive thickness anomalies in the center of the gyre (not shown). The atmospheric part of the SVD (Q'_H) shows a maximum in the Gulf Stream recirculation ([Fig. 14b](#)). The positive sign implies a warming, which acts on the negative SST anomalies. This indicates that Q'_H acts to damp the SST anomalies. The pattern of Q'_H is associated with the spatial distribution of SST anomalies. In this region, just south of the midlatitude jet where the mean cooling has its maximum (see [Fig. 2](#)), SST anomalies are easily generated by the stochastic heat flux forcing.

The response time of mode water to anomalous heat flux forcing of 13 months is the result of a storage mechanism (see HD98 for a detailed description). Anomalous cooling (heating) in the winter affects the stability of the water column. Due to shallow mixed layers in summer the anomalous stratification resides in the interior. In a subsequent winter, the mixed layer deepening is affected by the anomalous stratification. A more (less) stable stratification will lead to less (more) entrainment. Consequently, mode water will be more (less) voluminous. Also, the shallower (deeper) winter mixed layer leads to anomalous low (high) winter time SSTs. In this way SST anomalies reoccur from one winter to another. This process is enhanced by reentrainment of anomalously cold (warm) water.

The correlation between the time series of the second SVD pair peaks at a lag of 5 months ([Fig. 13](#)). The pattern of the oceanic part (mode water) of the SVD at this lag is single signed along the outcrop of mode water ([Fig. 15](#)). This is the signature of subduction at the outcrop. Anomalous mixed layer depths in the winter generate thickness anomalies in the mode water layer when the mixed layer detrains in spring. The signature is strongest when most detrainment has taken place, that is, in the summer. Furthermore, properties of the mixed layer are more sensitive to forcing in summer than in the winter, because summer mixed layers are relatively shallow. The anomalous wintertime forcing determines partly the mixed layer depth in summer.

A lag correlation analysis has been performed on the SVD pairs of SST and Q'_H as well. The results are shown in [Fig. 16](#). The first and the second SVD mode peak at a zero lag. The correlation between Q'_H and SST is higher than between Q'_H and the mode water thickness. The maximum at a zero lag confirms that the Q'_H responds to the SST anomalies. As shown above, Q'_H acts as a negative feedback. This is probably due to the relatively small scales in the model. For instance,

Drijfhout and Walsteijn (1998) show that the damping on the eddy scale is much larger than on the gyre scale. On larger scales than considered here, positive feedbacks between the ocean and the atmosphere may arise (e.g., [Latif and Barnett 1996](#)). The following picture emerges from the analysis. The stochastic heat flux excites SST anomalies in the mixed layer and anomalies in entrainment/detrainment. These modes are probably associated with linearly damped eigenmodes of the system ([Griffies and Tziperman 1995](#)). Here \dot{Q}'_H responds instantaneously to the anomalous SSTs and acts to reduce them. The thermal damping does not act directly on the interior stratification. The result is that in a following year the entrainment is affected by the anomalous stratification induced by the forcing the year before.

In [section 3b](#) we estimated the efficiency of the stochastic forcing in generating vertical velocity at the base of the mixed layer using the forcing spectra. It can easily be verified that, based on a white noise level of $1 \times 10^5 \text{ W}^2 \text{ m}^{-4}$, the stochastic heat flux is three times (in variance) as efficient as the stochastic freshwater flux. This difference cannot entirely account for the large amplitude (i.e., a factor of 3 instead of $(3)^{1/2}$) of mode water variability compared to the results presented in 3b.

Some short sensitivity experiments have been performed to elucidate the possible mechanisms for generating the stronger variability. It appeared that neither the seasonal cycle in stochastic forcing nor \dot{Q}'_H itself are responsible for the larger response. The variability increased when \dot{Q}'_H was set to zero and a pure heat flux forcing was applied instead. Also, we studied the role of convective adjustment, which has not been taken into account in the estimates in [section 3b](#) [according to [Eqs. \(11\)](#) and [\(12\)](#)]. We defined a convection index as the number of gridpoints during a month when convective adjustment takes place in the mixed layer. [Figure 17](#) shows the convection index for the experiments discussed in [sections 3a](#), [3b](#), and [3c](#). The index is based on 10 years of integration. As a reference, the convection index of a run without stochastic forcing is shown. Generally, most convection takes place in late winter when cooling is greatest. Although the differences are not large, most convection occurs in the stochastic heat flux experiment. This is consistent with the larger response found in the stochastic heat flux experiment compared to the response in the stochastic freshwater flux experiment. Also detrainment on an intermittent basis will occur more often when there is more convection. The vertical velocities associated with the detrainment are much larger than those estimated from [Eqs. \(11\)](#) and [\(12\)](#). This may explain the difference in the results of the stochastic freshwater flux and heat flux experiment.

An experiment with all stochastic forcings acting in concert has been performed as well. The stochastic heat flux dominates. The first EOF has a dipole pattern and accounts for 44% of the variance. This is identified as the heat flux driven variability. The second to fifth EOF patterns have wavelike signatures and account for 17%, 9%, 6%, and 5% respectively. These are signatures of the variability induced by the wind stress variations. The first SVD has a red noise spectrum and the second SVD peaks at 7 years (not shown). The timescale of 7 yr corresponds with the timescale found in stochastic wind stress experiment.

4. Summary and conclusions

In the present study the response of mode water to a white noise forcing is investigated. The same isopycnal model as used by HD98 has been forced by a stochastic forcing superimposed on the climatological forcing.

The stochastic wind stress forcing excites an internal mode in the ocean model. Planetary waves are excited at the eastern boundary and propagate through the westward return flow of the subtropical gyre. The period of the oscillation is 7 yr. This timescale is determined by the basin width and the wave propagation speed. Comparable modes of variability have been found in other models (e.g., [Zorita and Frankignoul 1997](#)). There is also observational evidence that long baroclinic waves cross the North Atlantic basin ([Polito and Cornillon 1997](#)). In the model, their role is small in generating mode water variability in the center of the gyre. Also, the amplitude of the thickness anomalies generated by the anomalous wind stress is small. However, frictional effects can be important.

The stochastic freshwater flux does not induce strong variability in the mode water layer of the model. No internal modes are excited. The largest response is found in the subduction region. The absence of a dynamic response of the gyre can be attributed to the nature of air-sea interaction and amplitude of the forcing spectra. An experiment with both stochastic wind stress and freshwater flux showed the same propagating waves as found in the stochastic wind stress experiment.

Finally, stochastic heat flux forcing has been applied. The response is substantial. A dipole mode dominates the variability in the mode water layer. SVD analysis shows that the dipole is forced by the stochastic heat flux. The heat flux generates SST anomalies. These are damped in the coupled model by the anomalous heat flux. Although the spatial variability in mode water is pronounced, the temporal variability exhibits a red noise response of the ocean to the white noise forcing.

The amplitudes of the variability induced by most of the stochastic forcings are rather small. The largest thickness anomalies are induced by the stochastic heat flux forcing. This forcing can generate mode water variability of the observed amplitude. The amplitude of the response may be underrated due to the idealized spatial structure of the stochastic forcing.

However, the applied stochastic forcing is spatially correlated. The range of spatial scales corresponds to the dominant spatial scales of variability over the North Atlantic region.

The time series of the observed potential vorticity shows regime shifts (e.g., [Talley and Raymer 1982](#); [Dickson et al. 1996](#)). Although the time series is rather short (1954–1991), the regime shifts suggest a dominant interannual to decadal timescale of variability. The stochastic heat flux can generate mode water variability of the observed timescale. However, [Fig. 12](#) shows that this timescale is not dominant. If the regime shifts in the observations are related to a significant peak at interannual to decadal timescales, the stochastic forcing experiments indicate that this peak should be the result of an (eddy-induced) internal mode, or it should be contained in the forcing. The latter can be the result of ocean–atmosphere interaction elsewhere in the North Atlantic, as proposed by [Dickson et al. \(1996\)](#).

Unfortunately, there are few observations of the spatial distribution of mode water variability to validate the patterns we found. In the model the spatial structure of the response to anomalous heat flux is distinctly different from the response to anomalous wind stress. The EOFs of temperature anomalies at 250 m presented by [Levitus et al. \(1994\)](#) hint toward planetary wave propagation. More observational evidence, however, is necessary to identify the spatial structure of subsurface modes of variability.

Acknowledgments

We thank Frank Selten for supplying us the subroutines to perform the statistical analyses and for introducing us to the OAF technique. Also the reviewers are acknowledged for their helpful suggestions and remarks on the manuscript. This research was supported by The Netherlands Organization for Scientific Research (NWO) Project VVA-770-03-252. The computations have been performed on the Fujitsu VPP-700 of the ECMWF in Reading.

REFERENCES

- Bleck, R., H. P. Hanson, D. Hu, and E. B. Kraus, 1989: Mixed layer–thermocline interaction in a three-dimensional isopycnic coordinate model. *J. Phys. Oceanogr.*, **19**, 1417–1439.. [Find this article online](#)
- , C. Rooth, D. Hu, and L. T. Smith, 1992: Salinity-driven thermocline transients in a wind- and thermohaline-forced isopycnic coordinate model of the North Atlantic. *J. Phys. Oceanogr.*, **22**, 1486–1505..
- Capotondi, A., and W. R. Holland, 1997: Decadal variability in an idealized ocean model and its sensitivity to surface boundary conditions. *J. Phys. Oceanogr.*, **27**, 1072–1093.. [Find this article online](#)
- Dickson, R., J. Lazier, J. Meincke, P. Rhines, and J. S. Swift, 1996: Long-term coordinated changes in the convective activity of the North Atlantic. *Progress in Oceanography*, Vol. 38, Pergamon, 241–295..
- Dorman, C. E., C. A. Paulson, and W. H. Quinn, 1974: An analysis of 20 years of meteorological and oceanographic data from ocean station N. *J. Phys. Oceanogr.*, **4**, 645–653.. [Find this article online](#)
- Drijfhout, S. S., 1994: On the heat transport by mesoscale eddies in an ocean circulation model. *J. Phys. Oceanogr.*, **24**, 353–369.. [Find this article online](#)
- , and F. H. Walsteijn, 1998: Eddy-induced heat transport in a coupled ocean–atmospheric anomaly model. *J. Phys. Oceanogr.*, **28**, 250–266.. [Find this article online](#)
- Fissel, P., S. Pond, and M. Miyake, 1976: Spectra of surface atmospheric quantities at ocean weather ship P. *Atmosphere*, **14**, 77–97..
- Flierl, G. R., 1978: Models of vertical structure and the calibration of two-layer models. *Dyn. Atmos. Oceans*, **2**, 341–381..
- Frankignoul, C., and P. Müller, 1979: On the generation of geostrophic eddies by surface buoyancy flux anomalies. *J. Phys. Oceanogr.*, **9**, 1207–1213.. [Find this article online](#)
- , —, and E. Zorita, 1997: A simple model of the decadal response of the ocean to stochastic wind forcing. *J. Phys. Oceanogr.*, **27**, 1533–1546.. [Find this article online](#)
- Griffies, S. M., and E. Tziperman, 1995: A linear oscillator driven by stochastic atmospheric forcing. *J. Climate*, **8**, 2440–2453.. [Find this article online](#)
- Hall, A., and S. Manabe, 1997: Can local linear stochastic theory explain sea surface temperature and salinity variability? *Climate Dyn.*, **13**, 167–180..

Hasselmann, K., 1976: Stochastic climate models. Part I. Theory. *Tellus*, **28**, 473–485..

Hazeleger, W., and S. S. Drijfhout, 1998: Mode water variability in a model of the subtropical gyre: Response to anomalous forcing. *J. Phys. Oceanogr.*, **28**, 266–288.. [Find this article online](#)

Jin, F. F., 1997: A theory of interdecadal climate variability of the North Pacific ocean–atmosphere system. *J. Climate*, **10**, 1821–1835.. [Find this article online](#)

Joyce, T. M., and P. Robbins, 1996: The long term hydrographic record at Bermuda. *J. Climate*, **9**, 3121–3131.. [Find this article online](#)

Latif, M., and T. Barnett, 1996: Decadal climate variability over the North Pacific and North America: Dynamics and predictability. *J. Climate*, **9**, 2407–2423.. [Find this article online](#)

Levitus, S., T. P. Boyer, and J. Antonov, 1994: *World Ocean Atlas. Vol 5: Interannual Variability of the Upper Ocean Thermal Structure*, NOAA Atlas NESDIS 5, U.S. Govt. Printing Office, 176 pp..

Luksch, U., and H. v. Storch, 1992: Modeling low frequency sea surface temperature variability in the North Pacific. *J. Climate*, **5**, 893–906.. [Find this article online](#)

Polito, P. S., and P. Cornillon, 1997: Long baroclinic Rossby waves detected by TOPEX/Poseidon. *J. Geophys. Res.*, **102**, 3215–3235..

Saravanan, R., and J. C. McWilliams, 1997: Stochasticity and spatial resonance in interdecadal climate fluctuations. *J. Climate*, **10**, 2299–2320.. [Find this article online](#)

—, and —, 1998: Advective ocean–atmosphere interaction: An analytical stochastic model with implications for decadal variability. *J. Climate*, **11**, 165–188.. [Find this article online](#)

Selten, F. M., R. J. Haarsma, and J. D. Opsteegh, 1999: On the mechanism of North Atlantic decadal variability. *J. Climate*, **12**, 1956–1973.. [Find this article online](#)

Talley, L. D., and M. E. Raymer, 1982: Eighteen degree water variability. *J. Mar. Res.*, **40** (Suppl), 757–775..

Weisse, R., U. Mikolajewicz, and E. Maier-Reimer, 1994: Decadal variability of the North Atlantic in an ocean general circulation model. *J. Geophys. Res.*, **99**, 12 411–12 421..

Wright, P. B., 1988: An atlas based on the “COADS” data set: Fields of mean wind, cloudiness and humidity at the surface of the global ocean. Max-Planck Report 14, Max-Planck-Institut, Hamburg, 70 pp. [Available from Max-Planck-Institut für Meteorologie, Bundesstr. 55, D-20146, Hamburg, Germany.].

Zorita, E., and C. Frankignoul, 1997: Modes of North Atlantic decadal variability in the ECHAM1/LSG coupled ocean–atmosphere general circulation model. *J. Climate*, **10**, 183–200.. [Find this article online](#)

APPENDIX

5. Optimal Autocorrelation Functions

Spatial and temporal variability of geophysical variables is often studied by expanding them into EOFs:

$$\psi_M(x, t) = \sum_{i=1}^M a_i(t)e_i(x),$$

where $e_i(x)$ are the eigenvectors (EOF patterns) of the covariance matrix of the field $\psi_M(x, t)$, and $a_i(t)$ are the principal components obtained from the projection of the field $\psi_M(x, t)$ onto the EOF patterns. EOF analysis resolves standing oscillations. However, EOFs are unable to resolve propagating phenomena, such as planetary waves. The physical interpretation of EOFs can therefore be difficult. In order to find propagating features a linear combination of the L principal components is searched:

$$b(t) = \sum_{i=1}^L c_i(t)a_i(t),$$

which maximizes the autocorrelation ρ at a certain lag τ :

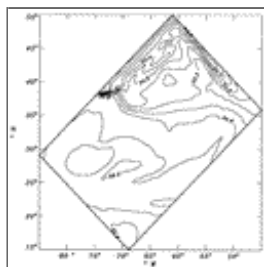
$$\rho_{\max} = \max \frac{\langle b(t)b(t + \tau) \rangle}{\langle b(t)b(t) \rangle}.$$

The angle brackets denote a time average. After some algebra, this variational problem can be solved. The field $\psi_L(x, t)$ can be expressed in terms of a set of patterns associated with the amplitudes $b_j(t)$:

$$\psi_L(x, t) = \sum_{i=1}^L \sum_{j=1}^L \lambda_i c_{ij} b_j(t) e_i(x) \equiv \sum_{j=1}^L b_j(t) f_j(x),$$

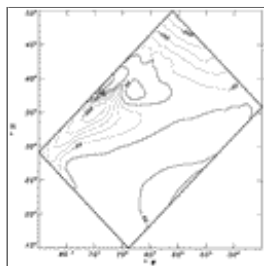
where λ_i are the eigenvalues of the corresponding EOFs. Finally, $f_j(x)$ are the optimal autocorrelation functions (OAFs), which are not orthogonal. Only the most dominant EOFs are used to determine the OAFs. Such a selection is necessary to avoid identification of patterns that account only for a minor part of the variance.

Figures



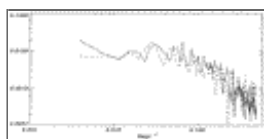
[Click on thumbnail for full-sized image.](#)

Fig. 1. Annually averaged sea surface salinity (psu).



[Click on thumbnail for full-sized image.](#)

Fig. 2. Averaged heat flux (in W m^{-2}) diagnosed from the run with restoring boundary conditions.



[Click on thumbnail for full-sized image.](#)

Fig. 3. Spectra of observed wind stress at 33°N , 22°W (solid line) obtained during the Subduction Experiment (daily sampled data from 6 Dec 1991 to 16 Dec 1993 courtesy of N. Brink, WHOI) and wind stress obtained with the stochastic forcing function [Eq. (6)] (stippled).



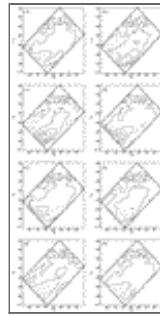
[Click on thumbnail for full-sized image.](#)

Fig. 4. Spectrum of the principal components of the first EOF of mode water thickness in the stochastic wind stress experiment.



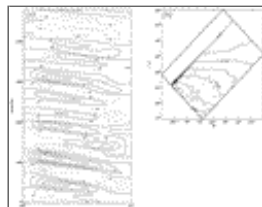
[Click on thumbnail for full-sized image.](#)

Fig. 5. Lagged correlations of eigenvalues of the OAF patterns of mode water thickness in the stochastic wind stress experiment.



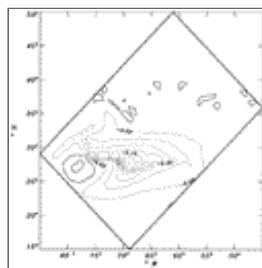
[Click on thumbnail for full-sized image.](#)

Fig. 6. Thickness anomalies in the mode water layer (m) obtained from OAF 4 and 5. The time between each panel is 11 months, which corresponds to 1/8 period.



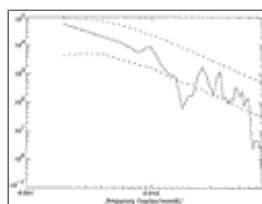
[Click on thumbnail for full-sized image.](#)

Fig. 7. (a) Time–latitude diagram of low-pass filtered thickness anomalies in mode water (note that the vertical axis corresponds to the shortened seasonal cycle). (b) Theoretically derived phase speed (m s^{-1}) of the first baroclinic Rossby mode away from topography.



[Click on thumbnail for full-sized image.](#)

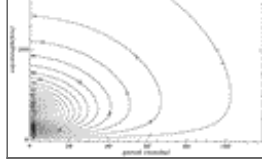
Fig. 8. First EOF of mode water thickness in the stochastic freshwater flux experiment.



[Click on thumbnail for full-sized image.](#)

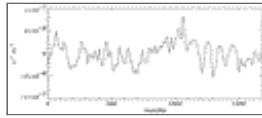
Fig. 9. Spectrum of principal components of the first EOF of mode water thickness in the stochastic freshwater flux experiment.





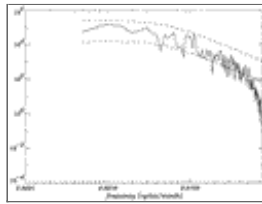
[Click on thumbnail for full-sized image.](#)

Fig. 10. Relative importance of stochastic freshwater flux forcing compared to stochastic wind stress forcing in generating vertical velocity (in terms of variance) at the base of the mixed layer as a function of wavelength (km) and period (months).



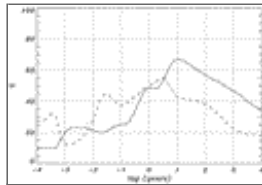
[Click on thumbnail for full-sized image.](#)

Fig. 11. Time series of potential vorticity (f/h) anomalies of the mode water layer at the models Panulirus Station in the coupled run with stochastic heat flux forcing.



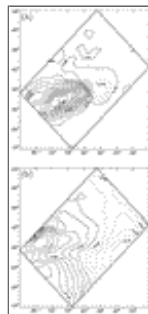
[Click on thumbnail for full-sized image.](#)

Fig. 12. Spectrum of the oceanic part of the first SVD mode of mode water thickness and anomalous heat flux (Q'_H) at a zero lag in the stochastic heat flux experiment.



[Click on thumbnail for full-sized image.](#)

Fig. 13. Lagged correlation between time series of Q'_H and mode water thickness of the first (solid) and second (dashed) SVD mode. Positive lags means that the anomalous fluxes lead the thickness anomalies in mode water in the stochastic heat flux experiment.



[Click on thumbnail for full-sized image.](#)

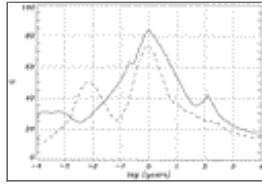
Fig. 14. First SVD mode of mode water thickness and anomalous heat flux (Q'_H) at a lag of 13 months (Q'_H leads) in the stochastic heat flux experiment. (a) Mode water thickness and (b) anomalous heat flux (Q'_H).





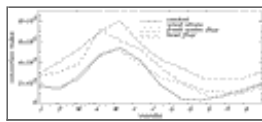
[Click on thumbnail for full-sized image.](#)

Fig. 15. Oceanic part of the second SVD mode of mode water thickness and anomalous heat flux (\dot{Q}'_H) at a lag of 5 months (\dot{Q}'_H leads) in the stochastic heat flux experiment.



[Click on thumbnail for full-sized image.](#)

Fig. 16. Lagged correlation between time series of SST and \dot{Q}'_H of the first (solid) and second (dashed) SVD mode. Positive lags mean that \dot{Q}'_H leads.



[Click on thumbnail for full-sized image.](#)

Fig. 17. Convection index (defined in [section 3c](#)) for the control experiment, stochastic wind stress forcing experiment ([section 3a](#)), stochastic freshwater flux forcing experiment ([section 3b](#)), and stochastic heat flux forcing experiment ([section 3c](#)).

¹ Talley and Raymer used a different definition for potential vorticity, i.e., $f/\bar{\rho} \Delta\rho/\Delta z$. In our model, the density differences between the isopycnal layers is proportional to $\alpha\Delta T$, with a temperature difference of 4°C. A value of $5 \times 10^{-8} \text{ m}^{-1} \text{ s}^{-1}$ in our model corresponds to $40 \times 10^{-14} \text{ s}^{-1} \text{ cm}^{-1}$ in their units.

Corresponding author address: Dr. Wilco Hazeleger, Royal Netherlands Meteorological Institute (KNMI), 3730 AE, P.O. Box 201, De Bilt, the Netherlands.

E-mail: hazelege@knmi.nl

[top ▲](#)



© 2008 American Meteorological Society [Privacy Policy and Disclaimer](#)
 Headquarters: 45 Beacon Street Boston, MA 02108-3693
 DC Office: 1120 G Street, NW, Suite 800 Washington DC, 20005-3826
amsinfo@ametsoc.org Phone: 617-227-2425 Fax: 617-742-8718
[Allen Press, Inc.](#) assists in the online publication of AMS journals.